Structural aspects of the glass-to-crystal transition in sodium-calcium silicate glasses

Henrik Bradtmüller[a], Mariana Carlos Villas-Boas[b], Edgar Dutra Zanotto[b], Hellmut Eckert[a,c,*]

[a] *Institut für Physikalische Chemie, WWU Münster, Corrensstraße 28/30, 48149 Münster, Germany*
[b] *Departamento de Engenharia de Materiais, Universidade Federal de São Carlos, CP 676, 13565-905, São Carlos, SP, Brasil*
[c] *Instituto de Física de São Carlos, Universidade de São Paulo, CEP 369, São Carlos, SP 13566-590, Brazil*

ABSTRACT

The structural aspects of the glass-to-crystal transition of Na_2O-$2CaO$-$3SiO_2$ (1-2-3) and $2Na_2O$-CaO-$3SiO_2$ (2-1-3) glasses have been investigated using X-ray diffraction and multinuclear NMR spectroscopy. These materials represent a small group of glasses that undergo homogeneous nucleation rather than following the thermodynamically favored path of surface crystallization. To understand this unusual nucleation mechanism the structural resemblance of the glasses and their isochemical crystals was probed on different length scales. Definitive evidence of structural similarity at the level of intermediate-range order is obtained from ^{23}Na spin echo decay experiments, which are sensitive to the spatial distribution of the sodium nuclei. In contrast the distributions of the silica network former units are quite different in the glassy and the crystalline states. These results suggest that a structural resemblance of the short- and intermediate-range order of the network modifiers rather than the network formers may be a key feature of homogeneously nucleating glasses.

1. Introduction

One of the fundamental issues in glass science is to understand the mechanisms and kinetics of crystallization processes. These are key to predict both the glass-forming ability of supercooled liquids and the uncontrolled crystallization (devitrification) during melt-cooling or glass heating. The latter two processes are of great relevance to science and technology alike, covering areas in pharmacy, geology, and materials science [1].

Most glasses and supercooled liquids, when annealed for sufficient time above or below their glass transition temperature, will exhibit nucleation of crystals, emanating from the sample surface or from solid impurities. This process is called heterogeneous nucleation [2,3]. In contrast, there is also the possibility of forming crystal nuclei from random structural fluctuations – a process called homogeneous nucleation. Although in principle, every supercooled liquid or glass should be able to follow the latter crystallization mechanism, to the present date only a small number of glasses are known to nucleate homogeneously. Even these glasses may follow the thermodynamically favored path of heterogeneous nucleation [4] if solid impurities or nucleation catalysts are present. To ensure homogeneous nucleation, which will lead to volume rather than surface crystallization, nucleation catalysts must be absent.

During the past 35 years, the physical properties and structural features of glasses undergoing homogeneous nucleation have been studied in great detail. This is for good reason, as internal homogeneous nucleation is the key to understanding the survival or death of the vitreous state. When the first critical nucleus is born, the supercooled liquid becomes unstable as crystal growth is a spontaneous process; hence, crystallization takes over.

The structural description of a glassy material can be addressed at various distinct ranges of length scale (see Fig. 1). *Short-range order* (SRO) typically describes the first atomic coordination sphere of a given atom: it comprises the identification and numbers of the directly bonded atoms, and the particular coordination geometry/symmetry. *Intermediate-range order* (IRO) describes the second coordination sphere, including the connectivity of individual coordination polyhedra and distance correlations between network formers and network modifiers. Finally *medium-range order* (MRO) describes larger structural units formed at the 1 nm scale, such as chain and ring structures or other extended aggregates which nevertheless pack randomly. We recently proposed that IRO and MRO might play a key role in facilitating homogeneous nucleation [5,6,7,8]. The kind and size of the formed units on this particular length scale might be directly related to the material's homogeneity and microscopic properties, which further determine stability against devitrification [9].

---

* Corresponding author at: Instituto de Física de São Carlos, Av. Trabalhador São Carlense 400, 13560-590 São Carlos, Brazil.
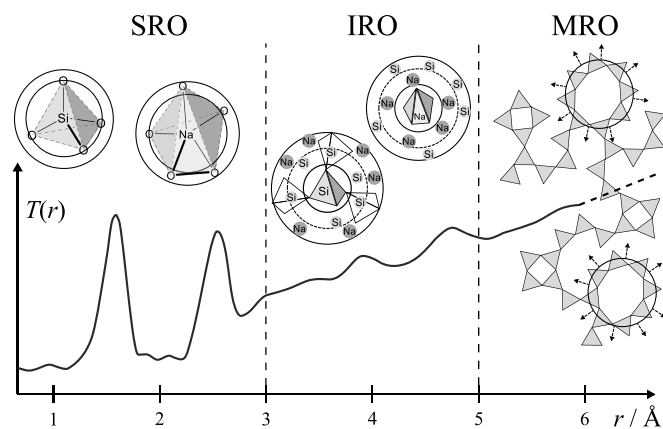*E-mail address:* eckerth@uni-muenster.de (H. Eckert).

Fig. 1. A Typical total distribution function $T(r)$ of a silicate glass, indicating the three length scale regimes in which glass structure is discussed: short-range order (SRO), intermediate-range order (IRO), and medium-range order (MRO) [5]. The total distribution function is related to the radial distribution function $g(r)$ via $T(r) = g(r) - 1$.

The experimental characterization of disordered materials on a length scale beyond SRO is challenging as commonly employed scattering methods are limited to compositionally simple systems. On the other hand, solid-state nuclear magnetic resonance (NMR) spectroscopy, owing to its element selectivity and inherently quantitative character, has already proven itself ideally suited for this task. In glass-ceramics, IRO and MRO have been most effectively probed employing magnetic dipole-dipole couplings involving the network modifier and network former species [10,11]. These dipolar couplings can be easily measured and related to interatomic distance distributions in a straightforward manner. For example, Longstaffe et al. have recently pointed out the suitability of the homonuclear ^{23}Na second moment $M_{2(Na-Na)}$ arising from the interatomic Na-Na distances as a means of quantifying structural similarity at the IRO / MRO level. Due to its inverse sixth power proportionality to the internuclear distance, the second moment is especially sensitive to the closest neighbor distances [12]. Experimentally, the homonuclear second moment can be measured by the spin echo decay method, where the normalized Hahn spin echo amplitude, $I(2\tau)/I(0)$ is measured by a 90°–τ–180°–τ pulse sequence as a function of the overall dipolar mixing time 2τ, during which the homonuclear magnetic dipole-dipole coupling interferes with echo formation. For a multi-spin system a Gaussian decay is expected [13], according to

$$\frac{I(2\tau)}{I(0)} = \exp\left[-\frac{M_2}{2}(2\tau)^2\right], \tag{1}$$

and various applications to distance distributions in glasses have been published [14]. In the present contribution we use the outlined approach to elucidate the IRO structural aspects of the glass-to-crystal transition in the Na$_2$O-CaO-SiO$_2$ system. Both of the chosen compositions, Na$_2$O-2CaO-3SiO$_2$ and 2Na$_2$O-CaO-3SiO$_2$, are known to nucleate homogeneously. To explore the overall structural relationship between the glassy state and the isochemical crystals, we complement these results by a comprehensive characterization of these glasses by high-resolution ^{29}Si and ^{23}Na solid-state NMR.

2. Experimental section

Sample Preparation and Characterization. Vitreous sodium-calcium silicates, Na$_2$O-2CaO-3SiO$_2$ (1–2–3) and 2Na$_2$O-CaO–3SiO$_2$ (2–1–3), were prepared by standard melt-cooling: Na$_2$CO$_3$ (Alfa Aesar, 98%), CaCO$_3$ (Sigma Aldrich, 99.9%), and SiO$_2$ (Vitrovita, 99.9%) were mixed in the desired ratios and then heated with a rate of 16 °C min^{-1} to 1400 °C, where the temperature was held for 4 h. The melt was cast,

crushed, and remelted three times for homogenization. After fast cooling small drops of the liquid by pressing between two steel plates, homogeneous and transparent pieces of glass were obtained and stored in a dry atmosphere.

The glass-ceramics were prepared via a two-step thermal treatment: For 1–2–3, the parent glass was heated to 505 °C and held at this temperature for 240 min to allow nucleation. Subsequently, the sample was heated to 569 °C to crystallize the material for 140 min. The 2–1–3 glass-ceramic was synthesized by heating for the same durations for nucleation and crystallization at temperatures of 594 and 659 °C, respectively. The glass-ceramics maintained the shape of their base glasses and were stored in a dry atmosphere. The specimens were subsequently characterized by X-ray diffraction (XRD) on a Rigaku Ultima IV diffractometer, operating with Cu Ka radiation, generated at 20 mA and 40 kV and integration times of 0.6 s at 0.02° steps. Diffraction data was compared against data from the Crystallogryphy Open Database (COD) [36].

Solid-State NMR. Single-resonance magic-angle spinning (MAS)-NMR spectra were recorded on a 5.7 T Varian 240-MR DD2, a 9.4 T Bruker DSX 400, and an 11.7 T Bruker DSX 500 spectrometer, using commercially available 2.5, 4.0 and 7.0 mm double and triple resonance magic-angle spinning (MAS) probes. ^{29}Si MAS NMR spectra were recorded at 5.7 and 9.4 T, with pulse durations of 5.0 and 3.5 μs at nutation frequencies of 50 and 71 kHz respectively, and a recycle delay of 700 s. The samples were spun at a MAS frequency of 5 kHz, and the chemical shifts are reported relative to tetramethylsilane using solid tetrakis(trimethyl silyl) silane (-9.8 ppm) as a secondary standard. ^{23}Na MAS NMR experiments were conducted at 9.4 T and a MAS frequency of 11.5 kHz. Pulse durations were about 0.5 μs at a nutation frequency of 100 kHz and recycle delays of 0.5 to 5.0 s were used. Chemical shifts are reported relative to 0.1 M NaCl solution using solid NaCl as a secondary standard (7.2 ppm relative to the solution). The MAS central transition lineshapes were fitted according to the Czjzek model [15], implemented within the DMFit data processing and simulation program [16]. ^{23}Na triple-quantum (TQ-)MAS experiments were recorded at 9.4 T (and 11.7 T), and a MAS frequency of 12.5 kHz using the same recycle delays as the MAS NMR experiments, and the standard z-filtered three-pulse sequence reported in reference [17]. The first two hard pulses were of 4.8 μs (5.1 μs) and 1.6 μs (2.0 μs) duration at a nutation frequency of 114 kHz (122 kHz), while for the detection a soft pulse of 10 μs duration at a nutation frequency of 12.5 kHz was used. The acquisition of the indirect dimension was synchronized with the rotor spinning speed, and dwell times of 1.25–5.0 μs (2.5 μs) were chosen for sampling in the indirect dimension. All data are shown after shearing transformation together with the sum projections of the high- and low-resolution spectra along the F1 and F2 axes respectively. The isotropic chemical shift δ_{iso}^{cs} and the second-order quadrupolar effect (SOQE) parameters were extracted from the centers of gravity in the F1 and F2 dimensions. Spin echo decay (SED) experiments were conducted at 11.7 T and a temperature of 190 K to eliminate any ^{23}Na ionic motion that could produce contributions to the echo decay from dynamic relaxation, which would tend to overestimate the second moment values. Sample containers with an outer diameter of 4.0 mm were filled only in the center third to reduce rf-inhomogeneities. A central transition (CT) nutation frequency of 15 kHz was found optimally suited for the experiments based on numerical simulations with the SIMPSON software package [18], and pulse durations of 8.4–8.6 and 16.1–16.5 μs were employed, respectively, for the selective excitation and refocusing pulses. The correct nutation frequency was ensured by comparison with the nutation behavior of solid NaCl and the exact pulse durations for the samples have been optimized prior to each experiment. While for a multi-spin system, the normalized amplitude of the spin echo $I(2\tau)/I(0)$ when measured as a function of dipolar mixing time is expected to follow Eq. (1) experimentally, one often finds that in disordered systems the Gaussian behavior is frequently only followed in the limit of relatively short dipolar mixing times. This is also the case with the
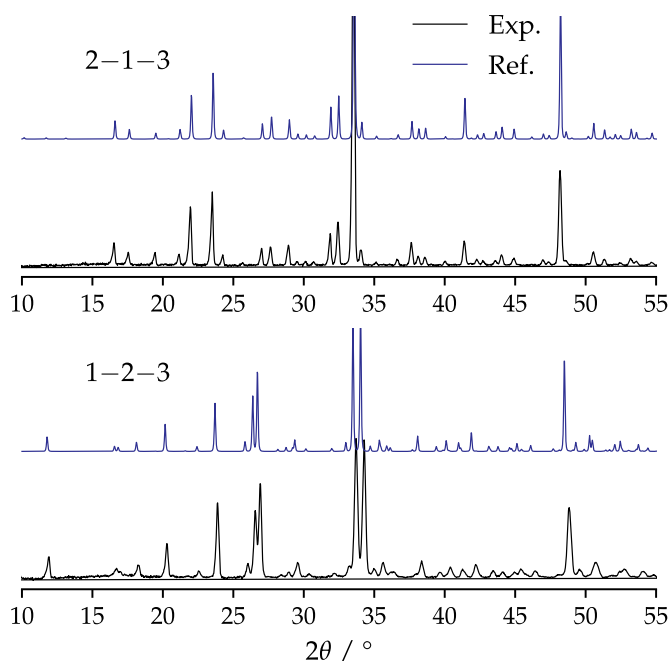
Fig. 2. Experimental (black lines) and reference (blue lines) powder X-ray diffraction patterns of combeite and crystalline $Na_4CaSi_3O_9$ obtained from the crystallization of the glassy samples of the present study. (For interpretation of the references to color in this figure legend, the reader is referred to the web version of this article.)

present samples, where the homonuclear second moments were determined from the Gaussian decay using linear regressions in the regime $0.01 \leq (2\tau)^2 \leq 0.04 \ ms^2$.

Fast decaying echo intensities in the very initial $(2\tau)^2$ regime up to a value of about $0.005 \ ms^2$ can be observed for all measurements; this part of the spin echo decay behavior was not considered in the analysis.

3. Results

X-ray powder diffraction. Fig. 2 shows the powder X-ray diffraction patterns of the crystalline 1–2–3 and 2–1–3 samples. Rather sharp reflexes were obtained for both samples, which do not indicate the presence of a residual glassy phase beyond the detection limit of approximately 5%. The diffraction pattern of 1–2–3 is in excellent agreement with reference data of the low-temperature phase combeite, $Na_2Ca_2Si_3O_9$, which crystallizes in the space group $P3_121$ [17], with lattice parameters a = 10.4649 Å; c = 13.1373 Å (rp = 6.865 rwp = 10.117). Compared to the literature values, (a = 10.4640 Å c = 13.1680 Å) a slight contraction of the unit cell can be noted. Likewise, the cubic lattice parameter for the crystalline 2–1–3 sample, space group Pa3 [18], a = 15.081 Å (rp = 11.945 rwp = 17.636), is in excellent agreement with the literature value of 15.0870 Å. The lattice parameter suggests a composition $Na_{3.90}Ca_{0.96}Si_3O_9$. All reflexes appear slightly broadened compared to the large-crystal reference data. Via the Scherrer approximation [21]

$$\mu = \frac{K\lambda}{FWHM \cos(\theta)}, \qquad (2)$$

the mean size of the ordered domains μ (smaller or equal to grain size) can be estimated from the FWHM of the most intense reflex. Here, $\lambda = 1.5406 \cdot 10^{-10}$ m is the wavelength of the Cu K_α X-rays and θ is the Bragg angle. Since the exact shape of the crystallites is unknown, a shape factor of K = 0.9 was assumed as a crude approximation. The analysis was performed for the main reflexes at $2\theta = 33.711°$ for 1–2–3 (FWHM = 0.31°) and $2\theta = 33.543°$ (FWHM = 0.22°) for 2–1–3, and yields mean sizes of (30 ± 10) nm and (50 ± 10) nm, respectively, for
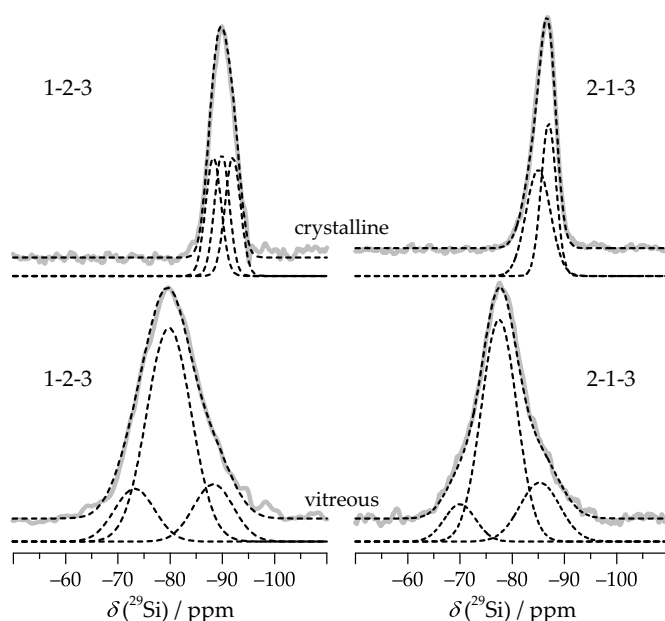

Fig. 3. ^{29}Si MAS NMR spectra of vitreous (bottom, recorded at 5.7 T) and crystalline samples (top, recorded at 9.4 T) of the 1–2–3 and 2–1–3 system including spectral deconvolutions (dashed lines).

the ordered domains of both samples. The reported error only reflects the accuracy of the determination of the reflexes' FWHM.

^{29}Si MAS NMR. Fig. 3 shows the ^{29}Si MAS NMR spectra of the vitreous and crystalline samples together with their lineshape deconvolutions. The spectra of the vitreous samples (bottom) bear close resemblance to each other, and a lineshape deconvolution was performed assuming three Gaussian components centered near -73, -80, and -88 ppm in the case of glassy 1-2-3 and -70, -78, and -85 ppm in the case of glassy 2-1-3. Within the experimental error, these shifts are identical to those recently reported in references [6] and [22] and can be assigned to $Si^{(1)}$, $Si^{(2)}$ and $Si^{(3)}$ units, with slightly varying line widths between 7 and 10 ppm. As expected from the composition, which indicates an average of two non-bridging oxygen atoms per silicon, $Si^{(2)}$ species make the dominant contribution, and the $Si^{(1)}$ and $Si^{(3)}$ signal area fractions are approximately equal (see Table 1).

Fig. 3, (top) demonstrates that the heat treatment of the vitreous precursor glasses for crystallization leads to significant spectroscopic changes. The crystalline samples exhibit signals which have much narrower linewidths and appear at significantly lower frequencies compared to their glassy counterparts. The structure of combeite (crystalline 1–2–3) is made up exclusively of $Si^{(2)}$ units forming six-

Table 1
^{29}Si lineshape simulation parameters, isotropic chemical shift δ_{iso}^{cs}, full width at half maximum, *FWHM*, and area fractions, of vitreous and crystalline 1–2–3 and 2–1–3 samples.

Sample	Unit	δ_{iso}^{cs} / ppm ± 0.5	*FWHM* / ppm ± 0.5	Area fractions /% ± 2%
1–2–3				
Glass	$Si^{(1)}$	−73.4	9.0	15
	$Si^{(2)}$	−80.0	10.0	68
	$Si^{(3)}$	−88.5	9.0	17
Crystal	$Si^{(2)}$	−88.3	3.5 ± 0.1	34
	$Si^{(2)}$	−89.9	3.3 ± 0.1	33
	$Si^{(2)}$	−92.0	3.5 ± 0.1	33
2–1–3				
Glass	$Si^{(1)}$	−70.0	7.0	10
	$Si^{(2)}$	−77.5	8.0	69
	$Si^{(3)}$	−85.3	9.0	21
Crystal	$Si^{(2)}$	−85.0	5.5 ± 0.1	53
	$Si^{(2)}$	−87.0	3.4 ± 0.1	47

H. Bradtmüller, et al.

membered rings that possess a two-fold symmetry. The crystal structure exhibits three distinct Si sites with equal populations, and thus, the ^{29}Si MAS NMR spectra were deconvoluted into three distinct signals accordingly. Under the constraint of equal linewidths and signal areas, an unambiguous three-component lineshape deconvolution can be found which is in good agreement with the experimental data. The crystal structure of $Na_4CaSi_3O_9$ comprises twelve-membered rings with three-fold symmetry axes, and crystal data shows the presence of two distinct crystallographic sites [18]. Consequently, the spectrum was deconvoluted with two Gaussian components in an approximate 1:1 ratio [22]. For both crystalline compounds, an assignment of the deconvolution components to the crystallographically inequivalent silicon sites is not possible in view of the small chemical shift differences and the fact that ^{29}Si chemical shifts are influenced by multiple parameters, including Si-O bond lengths, tetrahedral angle distortions, Si-O-Si bond angles [22–26] and relative number of Na vs. Ca neighbors. (see compilation of these structural details in Table S1 of the Supporting Materials Section). The situation is further complicated as both crystal structures contain various sites with mixed Na/Ca occupancies. Altogether, Fig. 3 does not suggest close structural resemblance between the short-range order of the network former silicon in the crystalline and glassy states. First of all, the glass contains multiple $Q^{(n)}$ sites, while the crystalline states are exclusively based on $Q^{(2)}$ units. Second, for both compositions the ~10 ppm chemical shift difference between the $Q^{(2)}$ sites in the glassy state and the $Q^{(2)}$ unit in the crystalline states, suggests great structural differences beyond the short-range order.

^{23}Na MAS and TQMAS NMR. Figs. 4 and 5 show the ^{23}Na MAS NMR spectra of the 1–2–3 and 2–1–3 samples respectively, before and after crystallization. Broad, asymmetric lineshapes are obtained on the glassy specimens, which can be simulated using the Czjzek distribution model. Simulations considering a single Czjzek component are found in excellent agreement with the spectra and suggest a high degree of disorder in the samples. Furthermore, isotropic chemical shifts of 7.6 and 11.0 ppm are obtained for 1–2–3 and 2–1–3 respectively, in agreement with the general trend that δ_{iso}^{cs} tends to increase with increasing Na content in silicate glasses [27]. This effect can be understood from the average sodium–oxygen distances, which decrease for increasing Na-content, as found for pure sodium silicate glasses.

Again, heat treatment for crystallization has a significant impact on the local ^{23}Na environments, recognizable by the significantly narrower signals for the crystalline samples. While the ^{23}Na signals of both samples show some structure, the overall rather featureless lineshapes render an unambiguous lineshape deconvolution difficult. The apparent disorder observed in these spectra reflect the mixed Na/Ca site
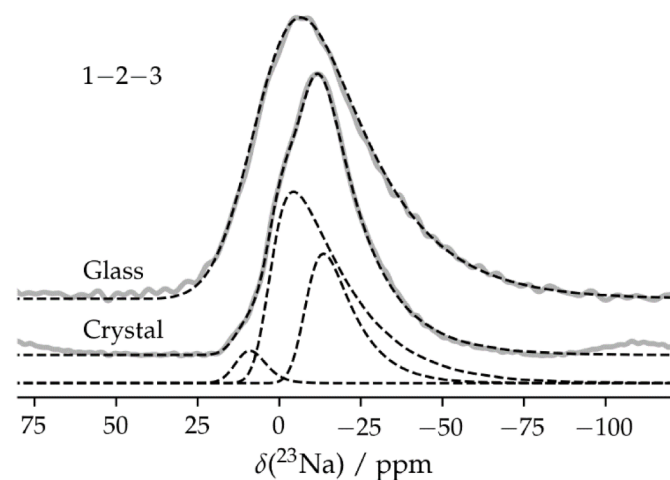

Fig. 5. ^{23}Na MAS NMR spectra of glassy and crystalline 2–1–3 at 9.4 T and a MAS frequency of 11.5 kHz. Dashed curves indicate simulations based on TQMAS spectra.
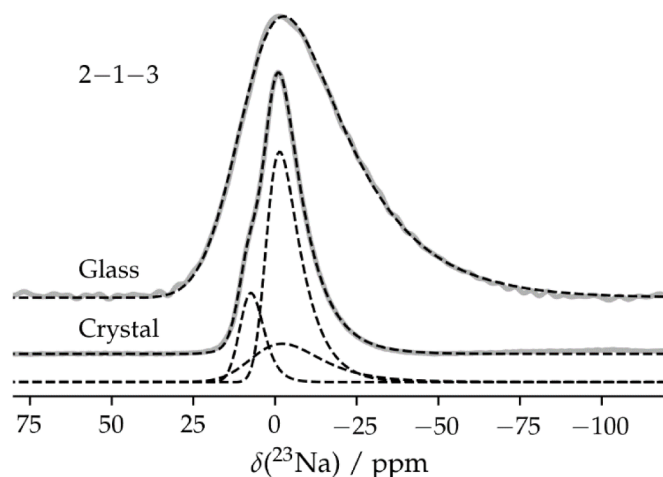
occupancies present in the crystal structure. This disorder creates a distribution of electric field gradients that will also affect the electric field gradients experienced by the ^{23}Na nuclei within the fully occupied Na sites in both structures. In a further attempt to improve resolution, TQMAS NMR studies were conducted on both the glassy and the crystalline samples. Fig. 6 (top) shows the results for glassy and crystalline 1–2–3. For the glass, the broadening alongside the isotropic dimension (indicated by the dashed diagonal) signifies a rather wide distribution of isotropic chemical shift values. The isotropic chemical shift and *SOQE* values were extracted from the centers of gravity in the isotropic and anisotropic spectral dimensions (F1/F2). Both parameters are in good agreement with the chemical shift values and average quadrupolar coupling constants used in the respective Czjzek simulation of the MAS-NMR signals. (Fig. 4, see Table 2).

The TQMAS NMR spectrum of crystalline 1–2–3 exhibits three differentiable sodium sites, A, B, and C, and the extracted isotropic chemical shifts and SOQE values are listed in Table 2. Based on the obtained parameters, a lineshape simulation was performed for the ^{23}Na MAS NMR spectrum, considering a Czjzek component for each of the three signals, allowing minor variations in the spectroscopic parameters. Fig. 4 displays the final fit result. It is important to note that the significant difference between the lineshape of the MAS NMR spectrum and the vertical projection of the TQMAS NMR spectrum upon F2 in Fig. 6 (bottom) arises from the non-quantitative character of the latter experiment, which is affected by the triple-quantum excitation efficiency. In the present case, the contribution of site B (having the largest C_Q value) to the vertical projection spectrum is rather low, while the quantitative ^{23}Na MAS NMR spectrum suggests that it is the dominating resonance signal. An assignment of these signals to the one fully occupied site Na3 and the three partly occupied sodium sites Na1, Na2, and Na4 in the crystalline compound is currently not possible.

The results obtained on the 2–1–3 system (Fig. 7) can be discussed analogously. While three lineshape components A', B', and C' can be identified in the crystalline compounds, their assignments to the fully occupied sites Na4 and Na5, and the three disordered Na/Ca sites are uncertain. Altogether, in neither of these two materials do the results suggest close resemblance between the ^{23}Na MAS or TQMAS results of the glassy versus the crystalline phases, but this may be due to the fact that ^{23}Na MAS NMR lineshapes in glasses (and also in disordered crystalline solids) are so strongly affected by electric field gradient distributions produced by the disorder. It is therefore difficult to use ^{23}Na MAS or TQMAS NMR for probing resemblance of short-range order. We note, however, that previous EXAFS experiments conducted on both the 1–2–3 and the calcium metasilicate glass systems have

Fig. 4. ^{23}Na MAS NMR spectra of glassy and crystalline 1–2–3 at 9.4 T and a MAS frequency of 11.5 kHz. Dashed curves indicate simulations based on TQMAS spectra.

proven very close resemblance of average cation coordination numbers and cation-oxygen distances [5,28]

^{23}Na spin echo decay spectroscopy: predicted behavior. A complementary experimental approach probing ordering/disordering phenomena on a larger distance scale involves the measurement of the average homonuclear ^{23}Na-^{23}Na dipole-dipole coupling strength. As the latter is rigorously calculable from structural models based on internuclear distance distributions, it presents an important quantitative criterion characterizing the spatial distribution of the sodium ions. The relevant quantity in question is the so-called dipolar second moment, which arises from the mean-squared average local field the ^{23}Na nuclei experience due to their magnetic moments of their neighbors. This quantity can be experimentally measured using spin echo decay spectroscopy, by analyzing Hahn spin echo amplitudes as a function of dipolar mixing times, expressed via Eq. (1). As previously shown, for spin-3/2 nuclei experiencing quadrupolar interactions the homonuclear second moment calculated for a central atom Na$_j$ is given by the expression [29,30]

Table 2
^{23}Na MAS NMR simulation parameters, i.e., isotropic chemical shift δ_{iso}^{cs}, average quadrupolar coupling constant $\bar{C}_Q$, and *SOQE* values, derived from the Czjzek fit and obtained from TQMAS experiments on vitreous and crystalline 1–2–3 and 2–1–3 samples.

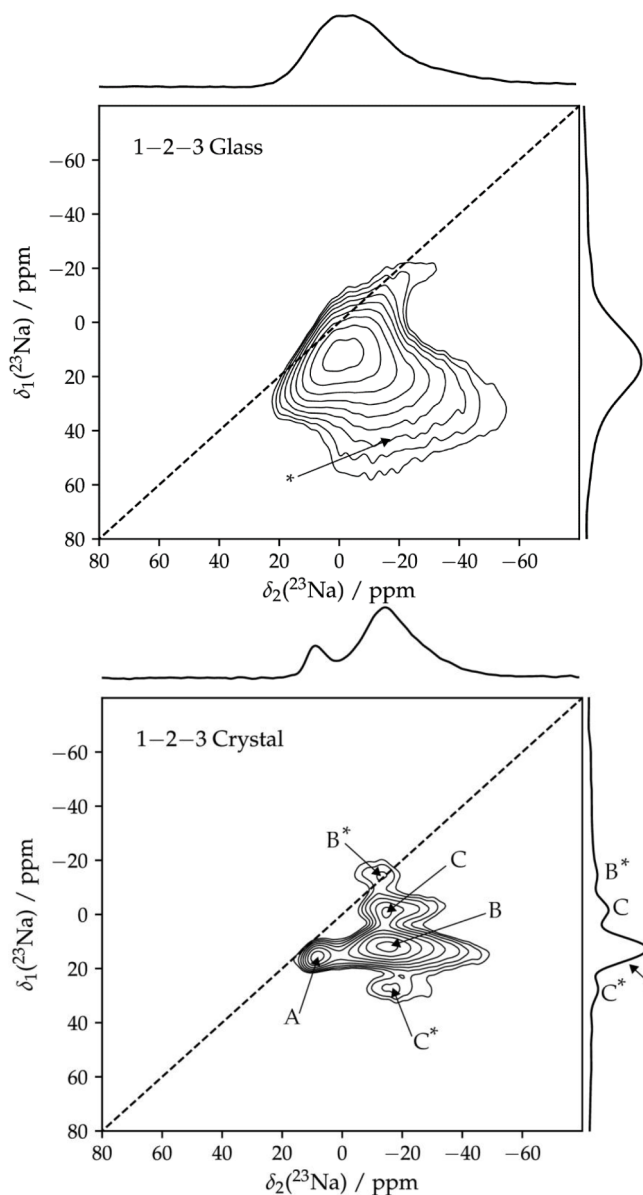| Sample	Site	δ_{iso}^{cs} / ppm ± 0.5		$\bar{C}_Q$ / MHz ± 0.1	*SOQE* / MHz ± 0.25	Area fractions / % ± 2%
		Czjzek	TQMAS	Czjzek	TQMAS	Czjzek
1–2–3 Crystal	A	12.0	12.3	1.5	1.8	5
	B	3.9	2.0	3.4	3.6	66
	C	−7.7	−8.5	2.5	2.7	29
Glass		7.6	7.1	2.9	2.8	100
2–1–3 Crystal	A'	10.0	9.5	1.2	1.0	17
	B'	6.5	10.4[a]	2.2	2.8[b]	21
	C'	2.9	2.3	1.7	1.6	62
Glass		11.0	10.3	2.9	2.9	100

[a] ± 1.5 ppm.
[b] ± 0.5 MHz.

Fig. 6. ^{23}Na TQMAS spectra of glassy (top, measured at 9.4 T) and crystalline (bottom, measured at 11.7 T) samples in the 1-2-3 system system recorded with the three-pulse, z-filter MQMAS sequence. The vertical dashed line indicates the isotropic dimension. Asterisks denote spinning-sidebands.

Fig. 7. ^{23}Na TQMAS spectra of glassy (top, measured at 9.4 T) and crystalline (bottom, measured at 11.7 T) in the 2–1–3 system recorded with the three-pulse, z-filter TQMAS sequence. The vertical dashed line indicates the isotropic dimension. Asterisks denote spinning sidebands.
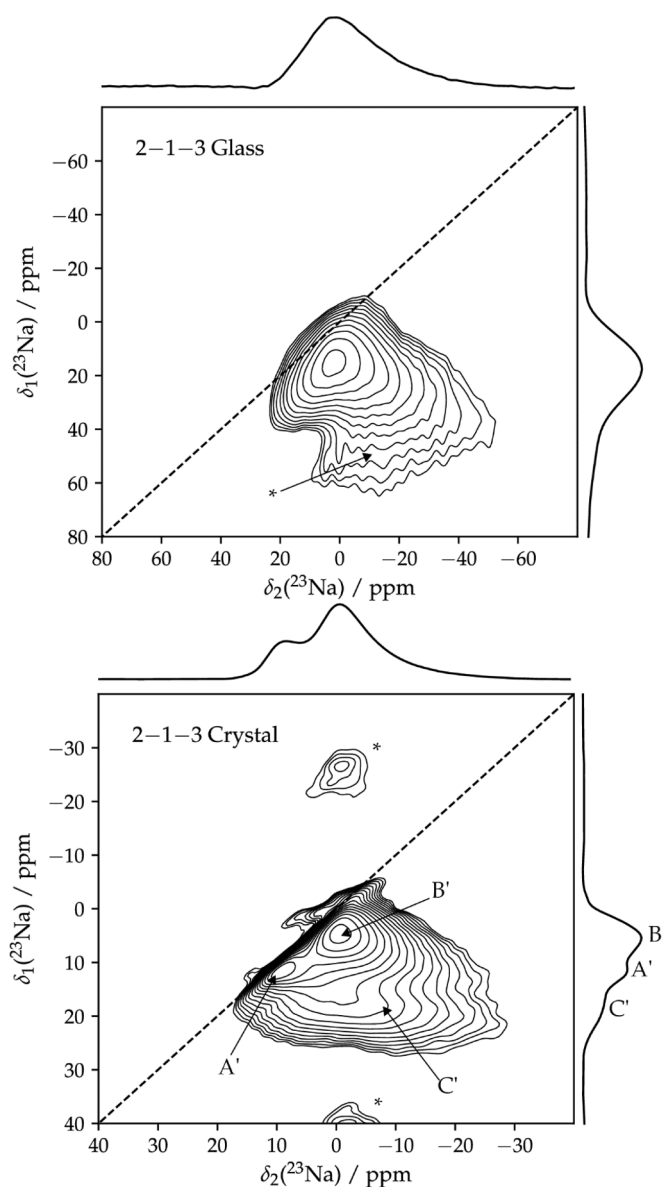
Table 3

Calculated second moments $M_{2(Na\text{-}Na)}$ for the glassy and crystalline samples of the systems 1–2–3 and 2–1–3, and ^{23}Na site occupancy p for the crystalline compounds.

Sample	p		$M_{2(Na\text{-}Na)}$/ 10^6 rad^2 s^{-2}	
	1–2–3	2–1–3	1–2–3	2–1–3
Calculated				
Na1	0.42	0.72	6.76	10.33
Na2	0.17	0.13	6.91	14.61
Na3	1.00	0.94	4.78	19.10
Na4	0.41	1.00	6.28	10.34
Na5	–	1.00	–	9.91
Average			5.60	12.20[a]

[a] value calculated based on a total Na stoichiometry of 3.9 atoms per formula as powder diffraction data suggests a stoichiometry of $Na_{3.9}Ca_{0.96}Si_3O_9$, rather than $Na_4CaSi_3O_9$.

$$< M_{2(Na-Na)} > \; = \; 0.9562 \left(\frac{\mu_0}{4\pi} \right)^2 \hbar^2 \gamma_{Na}^4 \sum_{i \neq j} r_{ij}^{-6}, \tag{3}$$

where μ_0 is the vacuum magnetic permeability constant, $\hbar = h/2\pi$ is the reduced Planck constant, γ_{Na} the gyromagnetic moment of the ^{23}Na nuclei, and r_{ij}^{-6} denote the inverse sixth power of the internuclear distances of the observed sodium atoms j and all the surrounding Na^+ ions i. To calculate $< M_{2(Na-Na)}>$ for a crystalline compound, a weighted average over all crystallographically inequivalent sodium sites Na_j must be taken, counting all the Na–Na distances r_{ij} up to a certain convergence limit. This latter limit is typically reached at four times the shortest internuclear distance. If some of the Na sites in the vicinity of a central sodium atom are only partially occupied (as is the case in the present materials with Na/Ca mixing on certain sites), this partial occupancy has to be taken into account by a linear scaling factor for that particular contribution. For calculating $M_{2(Na-Na)}$ for a particular glass structural model, Eq. (3) has to be applied to and averaged over a sufficiently representative number of central sodium ions, until the result will no longer depend on the number of sodium ions over which the result is being averaged.

The expected ^{23}Na second-moment values of combeite and $Na_4CaSi_3O_9$ can be calculated from the crystal structure data [19,20] and serve as a point of reference to the experimental results. Information of the unit cells derived from powder diffraction data shows that both crystalline compounds possess multiple ^{23}Na crystallographic sites which are partly shared with calcium atoms [19,20]. To calculate the btotal homonuclear ^{23}Na second moment values for both materials, it is necessary to consider the sodium site occupancies as weighting factors in the calculation of the individual second moment of each site. Generally, the second moment of any ^{23}Na site Na_j is calculated from Eq. (3) considering that

$$M_{2(Na-Na)}(Na_j) = \sum_{i=1}^{N} [M_2(Na_i - Na_j) \cdot p(Na_i)], \tag{4}$$

where i is iterated over all existing sites N and $p(Na_i)$ is the respective occupancy factor. The total second moment of the material is then the second moment sum over all crystal sites Na_j weighted by p which is expressed by.

$$M_{2(Na-Na)}(total) = \left(\frac{1}{N} \right) \sum_{j}^{N} M_2(Na_j) p(Na_j) \tag{5}$$

Table 3 lists all crystallographic sites from diffraction data, together with their occupancies, their individual calculated second moment value and the derived average second moment values for 1–2–3 and 2–1–3. The calculations outlined above result in a predicted average $M_{2(Na-Na)}$ value of $5.60 \cdot 10^6$ rad^2 s^{-2} for combeite (1–2–3) and $12.20 \cdot 10^6$ rad^2 s^{-2} for 2–1–3 reflecting its twice as high total sodium content.

^{23}Na spin echo decay spectroscopy: experimental considerations. While the Gaussian decay of spin echo amplitude as a function of dipolar mixing time 2τ, as predicted by Eq. (1) has been frequently verified for multispin systems containing spin-1/2 nuclei [14], this approach is more complicated for the case of quadrupolar nuclei such as ^{23}Na (spin-3/2). Even so, this method has been quite successful in measuring homonuclear second moments $M_{2(I-I)}$ for distributions of spin-3/2 nuclei in the past [29]. Applications to quadrupolar nuclei appear problematic at first, as the quadrupolar Hamiltonian, like that of the homonuclear dipole coupling, is bi-linear in I_z, and is thus expected to contribute to the evolution of the density matrix. Despite this fundamental problem, it was previously shown that an extension of this method to quadrupolar nuclei is possible in the weak irradiation limit, where to a good approximation only the central $m = \frac{1}{2} \Leftrightarrow m = -\frac{1}{2}$ transition, which is not affected by quadrupolar interactions, is being observed (pseudo-spin-½ situation) [29,30]. This limit is attained if the nutation frequency ν_1 is significantly smaller than the quadrupolar frequency $\nu_Q = 3C_Q/2I(2I\text{-}1)$, where C_Q is the nuclear electric quadrupolar coupling constant in frequency units. Maintaining this condition, we found good agreement between experimental and calculated $M_{2(Na-Na)}$ values for a number of crystalline sodium compounds [29,31]. Based on extensive simulations carried out recently in our laboratory on the spin echo decay behavior of ^{23}Na-^{23}Na two-spin systems the accuracy of the method is found to depend on the strength of the dipole-dipole coupling to be measured as well as on second-order quadrupolar effects affecting the lineshape of the central transition [31]. These simulations show that reliable ^{23}Na second moment values can be obtained within 10–20% accuracy under the condition $H_Q^{(1)} > H_1 > H_D$
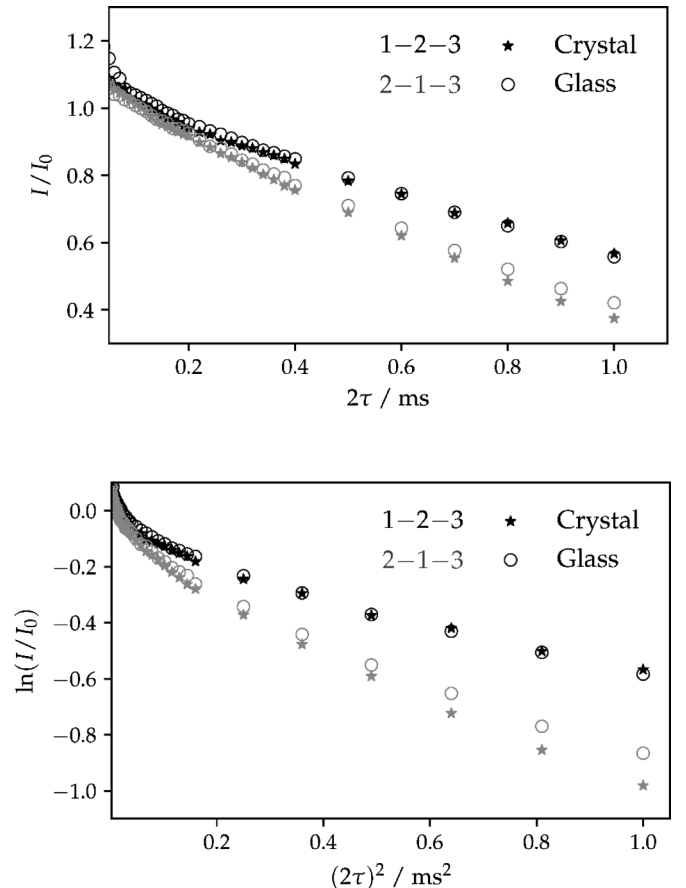

Fig. 8. Overview of the ^{23}Na SED curves in the four samples under study. Top: Plot of normalized spin echo amplitude versus 2τ. Bottom: plot of $\ln(I(2\tau)/I(0))$ versus $(2\tau)^2$, showing the deviation from Gaussian behavior more clearly.

ARTICLE IN PRESS

H. Bradtmüller, et al.   Journal of Non-Crystalline Solids 532 (xxxx) xxxx
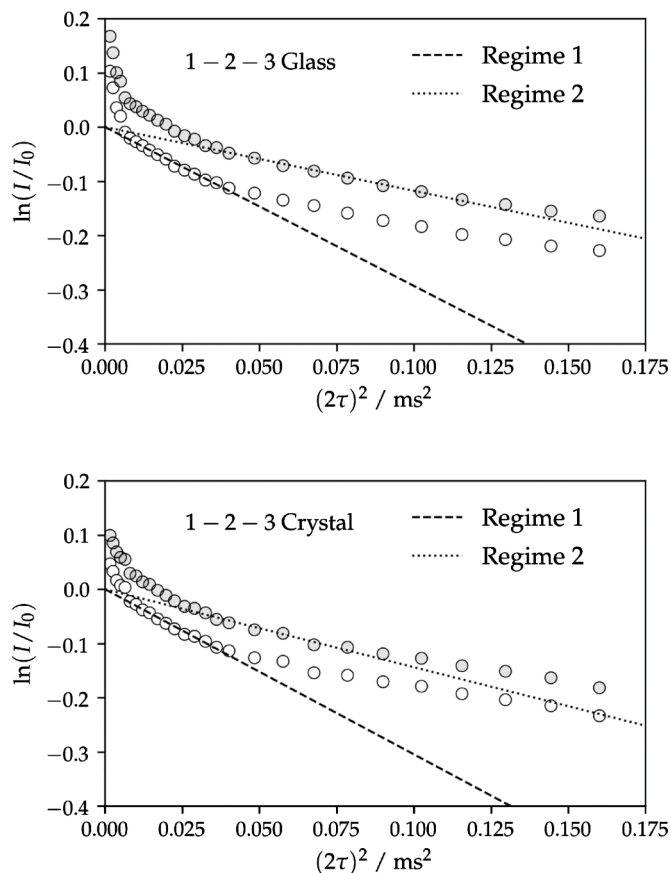
Fig. 9. Static ^{23}Na SED curves of glassy (top) and crystalline (bottom) samples in the system 1–2–3. The measurements were performed at B_0 = 11.7 T and 190 K. The open and gray circles depict the same dataset normalized to the ordinate intercept of a linear fit in the regime of short dipolar mixing times (regime 1, black dashed line) and higher dipolar mixing times (regime 2, dotted line) respectively. The shift along the vertical axis was undertaken to illustrate the two regimes of analysis more clearly.

Fig. 10. Static ^{23}Na SED curves of glassy (top) and crystalline (bottom) samples in the system 2–1–3. The measurements were performed at B_0 = 11.7 T and 190 K. The open and gray circles depict the same dataset normalized to the ordinate intercept of a linear fit in the regime of short dipolar mixing times (regime 1, black dashed line) and higher dipolar mixing times (regime 2, dotted line). The shift along the vertical axis was undertaken to illustrate the two regimes of analysis more clearly.

~ $H_Q^{(2)}$ < 5 kHz, where H_1, H_D, $H_Q^{(1)}$ and $H_Q^{(2)}$ denote the Hamiltonians representing the nutation, homonuclear dipole-dipole coupling, and first- and second-order quadrupolar perturbation energies, respectively. It was found that the spin exchange becomes significantly suppressed in the regime of experimental evaluation (($(2\tau)^2$ < 0.04 ms^2) for CT linewidths exceeding 5 kHz, leading to strong M_2 underestimation [29]. This situation does, however, not apply to the present samples.

Considering the information summarized in Table 3, extensive simulations are required to ensure the use of experimental measurement conditions that maintain the quantitative character of the spin echo decay approach for any combination of magnetic dipole-dipole coupling strength (Table 3 indicates a total range of $M_{2(Na-Na)}$ values between 4 and 20 × 10^6 rad^{2}s^{-2}) for the sodium sites and nuclear electric quadrupolar coupling constants (C_Q = 1–4 MHz based on our present results). We find that this condition will be fulfilled if an external magnetic field of 11.7 T and nutation frequencies of 15 to 20 kHz are used [31].

^{23}Na spin echo decay spectroscopy: experimental results. Fig. 8 presents the experimental results obtained on the glassy and the crystalline samples. For either composition, we clearly notice a very close resemblance of the results obtained before and after crystallization. Owing to the higher sodium ion content (and hence the stronger homonuclear dipole-dipole couplings), the spin echo intensity of the 2–1–3 samples decays significantly faster compared to that of the 1–2–3 samples.

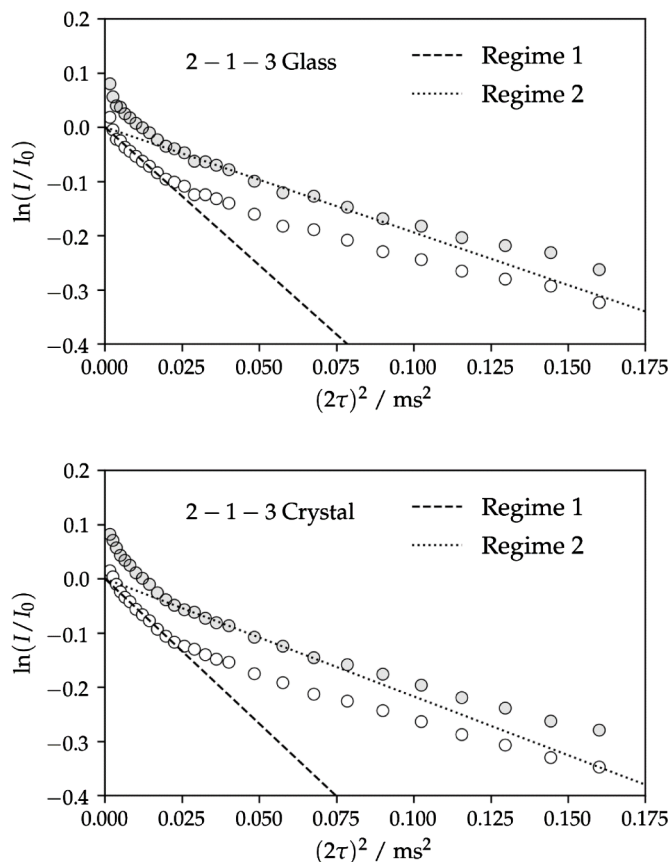The semilogarithmic plot of echo amplitude versus $(2\tau)^2$ reveals that

the overall decays show clear deviations from Gaussian behavior, making it necessary to discuss different time regimes. These regimes are shown in Figs. 9 and 10 for each of the glassy and the crystalline samples, and Table 4 summarizes the second moment values obtained for both of these regimes from linear regressions according to Eq. (1). Each part of Figs. 9 and 10 shows two plots created from the identical data set: Data depicted by open circles have been normalized to the intensity of the linear regression at $(2\tau)^2$ = 0 made in the initial regime 1 (0.01 ≤ $(2\tau)^2$ ≤ 0.04 ms^2, black-dotted line). This regime was previously identified as the one in which quantitatively reliable $M_{2(Na-Na)}$ values can be measured in crystalline model compounds [29]. In the present study we can identify a second regime (regime 2) spanning the range 0.04 ≤ $(2\tau)^2$ ≤ 0.1 ms^2, and data depicted by gray filled circles are normalized to the intercept of the vertical axis of the linear regression made from those data points. The result reveals that within regime 1 the $M_{2(Ma-Na)}$ values of the glasses and the isochemical crystalline compounds are identical within experimental error for both compositions, and are moreover in excellent agreement with the theoretically predicted values for the crystalline compounds. The close resemblance between glass and crystal even extends to Regime 2, even though the apparent $M_2'_{(Na-Na)}$ values obtained here cannot be interpreted from a structural viewpoint in a straightforward way. In this more extended time regime, the spin echo intensity evolution is additionally influenced by higher moments.

Table 4
Experimentally obtained and calculated second moment values $M_{2(Na\text{-}Na)}$ (± 10%) in units of 10^6 rad^{2}s^{-2} for the glassy and crystalline samples of the systems 1–2–3 and 2–1–3. The numbers in parentheses refer to the apparent $M_{2(Na\text{-}Na)}$ values obtained for the longer-term Regime 2.

Sample		$M_{2(Na\text{-}Na)}$ (exp)	$M_{2(Na\text{-}Na)}$ (calc)
1–2–3	cryst.	6.1(2.4)	5.60
1–2–3	glass	5.9(2.9)	
2–1–3	cryst.	10.7(4.4)	12.20
2–1–3	glass	10.2(3.9)	

4. Discussion

From the results illustrated above we may conclude that – even though it is difficult to assess from the ^{23}Na chemical shifts and quadrupolar coupling constants how close the local coordination environments of the sodium ions are – in the glasses and their isochemical crystals, the overall spatial distributions of the sodium ions remain very close to each other before and after crystallization. As previously discussed, this observation is common to that observed in glassy systems prone to homogeneous nucleation: the network modifier species in them have strikingly similar aspects of medium range order regarding their overall distribution in space [5].

Fig. 11 puts the results of the present study into the context of previous work, plotting the change of M_2 upon glass crystallization relative to its value in the crystalline phase, i.e., the parameter $\left| \Delta M_2 / M_{2c} \right|$ for homogeneously and heterogeneously nucleating systems. In this plot, the second moments only refer to dipole-dipole couplings involving the network modifier ions, describing interactions with each other, i.e. only data relating to Li-Li or Na-Na interactions are being considered. Note that for the heterogeneously nucleating glasses sodium disilicate (NS$_2$) [12], albite (NAS$_6$ - NaAlSi$_3$O$_8$) [5] and sodium diborate (NB$_2$) [5,32] the $M_{2(Na\text{-}Na)}$ values differ substantially between the glassy and crystalline states, whereas rather small values of $\left| \Delta M_2 / M_{2c} \right|$ are observed in the homogeneously nucleating sodium calcium silicate (NCS$_3$) glasses of the present study. The relative change of $M_{2(Na\text{-}Na)}$ upon crystallization is much closer to the analogous $M_{2(Li\text{-}Li)}$ numbers found for lithium disilicate (LS$_2$) and lithium diborate (LB$_2$) glasses, both of which show homogeneous nucleation behavior. The results further suggest that the interionic Coulomb repulsion plays a significant role in dominating the structural organization of homogeneously nucleating glasses near the glass transition temperature.

The present findings reinforce the previously-stated concept that similar short- and intermediate-range order in the glassy and crystalline states for the network modifying species facilitates homogeneous nucleation. Owing to inherent limitations caused by the distribution of quadrupolar coupling parameters and their effects upon the spectra, ^{23}Na MAS and TQMAS NMR are found to be generally less suitable for an assessment as to how similar the sodium local environments in sodium-calcium silicate glasses and their isochemical crystals are. However, a close resemblance had been already previously noted for these materials from EXAFS experiments [5,28]. Definitive support for the above hypothesis comes from the ^{23}Na spin echo decay experiments reported in the present study, which suggest that the overall spatial distributions of the sodium ions in these glasses and their isochemical crystals are very similar. These findings agree well with early neutron diffraction studies [33] and molecular dynamics simulations [34] on calcium metasilicate glass, where both the local environment and the spatial Ca^{2+} ion distribution were found to correspond closely to that in the crystalline state, and even evidence of nanometer-scale ordering was found in this homogeneously nucleating material. Further evidence comes from in-situ high-temperature X-ray diffraction (XRD) experiments coupled with partial radial distribution function analysis of a CaO–Al$_2$O$_3$–SiO$_2$ glass, where it was shown that, in the initial stages of crystallization, the Ca^{2+} ions rearrange much faster than the network formers, Al and Si [35].
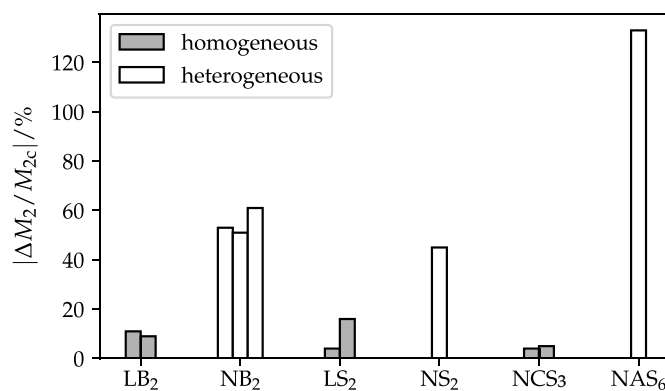

Fig. 11. Graphical distinction of $\left| \Delta M_2 / M_{2c} \right|$ data relating to the spatial distribution of the modifier cations for glasses undergoing homogeneous and heterogeneous nucleation, respectively. Glasses: Li$_2$O·2B$_2$O$_3$ (LB$_2$), Na$_2$O·2B$_2$O$_3$ (NB$_2$), Li$_2$O·2SiO$_2$ (LS$_2$), Na$_2$O·2SiO$_2$ (NS$_2$) and Na$_2$O·Al$_2$O$_3$·6SiO$_2$ (NAS$_6$), (all the data from reference [5]); NCS$_3$: Na$_2$O·2CaO·3SiO$_2$ and 2Na$_2$O·CaO·3SiO$_2$ (data from present work).

5. Conclusions

The present findings evidence intermediate range order similarities between the glassy and crystalline states in sodium calcium silicate glasses despite the differences in local order at the atomic scale indicated by ^{29}Si MAS NMR experiments. They reinforce the previously-stated concept that glasses having the structural arrangement of the network modifiers similar to the arrangement in their isochemical crystal phase are more likely to undergo internal, homogeneous, nucleation than glasses/crystals that show significant differences in this regard. These findings corroborate the idea that the short- and intermediate-range order of the network modifiers is the key parameter in determining the nucleation mechanism, whereas other aspects (e.g., concerning short-range order and connectivity of the network formers) are less relevant.

CRediT authorship contribution statement

Henrik Bradtmüller: Data curation, Formal analysis, Investigation, Methodology, Validation, Visualization, Writing - original draft, Writing - review & editing. **Mariana Carlos Villas-Boas:** Investigation, Methodology. **Edgar Dutra Zanotto:** Conceptualization, Funding acquisition, Project administration, Resources, Writing - review & editing. **Hellmut Eckert:** Conceptualization, Funding acquisition, Project administration, Resources, Supervision, Validation, Writing - original draft, Writing - review & editing.

Declaration of Competing Interest

The authors declare that they have no known competing financial interests or personal relationships that could have appeared to influence the work reported in this paper.

Supplementary materials

Supplementary material associated with this article can be found, in the online version, at doi:10.1016/j.jnoncrysol.2019.119844.

References

[1] E.D. Zanotto, Int. J. Appl. Glass Sci 4 (2013) 117–124.

[2] W. Höland, V. Rheinberger, M. Schweiger, Phil. Trans. R. Soc. Lond. A 361 (2003) 575–589.

[3] L.A. Souza, M.L.G. Leite, E.D. Zanotto, J. Non-Cryst. Solids 351 (2005) 3579–3586.

[4] A.S. Abyzov, V.I. Fokin, E.D. Zanotto, J. Non-Cryst. Solids 500 (2018) 231–234.

[5] E.D. Zanotto, J.E. Tsuchida, J.F. Schneider, H. Eckert, Int. Mater. Sci. Rev. 60 (2015) 376–391.

[6] J. Schneider, V.R. Mastelaro, H. Panepucci, E.D. Zanotto, J. Non-Cryst. Solids 273 (2000) 8–18.

[7] E.D. Zanotto, E. Müller, J. Non-Cryst. Solids 130 (1991) 220–221.

[8] J. Deubener, J. Non-Cryst. Solids 273 (2005) 1500–1511.

[9] J.W Zwanziger, J.C. McLaughlin, S.L. Tagg, Phys. Rev. B 56 (1997) 5243–5249.

[10] J.C. McLaughlin, S.L Tagg, J.W Zwanziger, D.R. Haeffner, S.D. Shastri, J. Non-Cryst. Solids 274 (2000) 1–8.

[11] E.M. Ratai, M. Janssen, J.D. Epping, J.C.C. Chan, H. Eckert, Phys. Chem. Glasses 44 (2003) 45–53.

[12] J.G. Longstaffe, U. Werner-Zwanziger, J.F. Schneider, M.L.F. Nascimento, E.D. Zanotto, J.W. Zwanziger, J. Phys. Chem. C 112 (2008) 6151–6159.

[13] D. Lathrop, D. Franke, R. Maxwell, T. Tepe, R. Flesher, Z. Zhang, H. Eckert, Solid State Nucl. Magn. Reson 1 (1992) 73–83.

[14] H. Eckert, Progr. Nucl. Magn. Reson. Spectrosc 24 (1992) 159–293.

[15] J.-.B d'Espinose de Lacaillerie, C. Fretigny, D. Massiot, J. Magn. Reson 192 (2008) 244–251.

[16] D. Massiot, F. Fayon, M. Capron, I. King, S.L. Calve, B. Alonso, J.O. Durand, B. Bujoli, Z. Gan, G. Hoatson, Magn. Reson. Chem. 40 (2002) 70–76.

[17] J.P. Amoureux, C. Fernandez, S. Steuernagel, J. Magn. Reson. A 123 (1996) 116–118.

[18] M. Bak, J.T. Rassmussen, N.C. Nielsen, J. Magn. Reson. 147 (2000) 296–330.

[19] H. Ohsato, Y. Takeuchi, Acta Crystallogr. C42 (1986) 934–937.

[20] R.X. Fischer, E. Tillmans, Z. Kristallogr. 166 (1994), 245–256.

[21] A.L. Patterson, Phys. Rev. 56 (1939) 978–982.

[22] J.F. Schneider, V.R. Mastelaro, E.D. Zanotto, B.A. Shakhmatkin, N.M. Vedishcheva, A.C. Wright, H. Panepucci, J. Non-Cryst. Solids 325 (2003) 164–178.

[23] B.L. Sheriff, H.D. Grundy, Nature 332 (1988) 819–822.

[24] M.R. Hansen, H.J. Jakobsen, J. Skibsted, Inorg. Chem. 42 (2003) 2368–2377.

[25] A. Sebald, L.H. Merwin, W.A. Dollase, F. Seifert, Phys. Chem. Minerals 17 (1990) 9–16.

[26] A. Pedone, T. Charpentier, M.C. Menziani, Phys. Chem. Chem. Phys. 12 (2010) 6054–6066.

[27] X. Xue, J.F. Stebbins, Phys. Chem. Minerals. 20 (1993) 297–307.

[28] V.M. Mastelaro, E.D. Zanotto, N. Lequeux, R. Cortès, J. Non-Cryst. Solids 262 (2000) 191–199.

[29] B. Gee, H. Eckert, Solid State Nucl. Magn. Reson. 5 (1995) 113–122.

[30] J. Haase, E. Oldfield, J. Magn. Reson. A 101 (1993) 30–40.

[31] H. Bradtmüller, Ph.D. thesis, Westfälische Wilhelms-Universität Münster, 2019.

[32] B. Chen, U. Werner-Zwanziger, J.W. Zwanziger, M.L.F. Nascimento, L. Ghussn, E.D. Zanotto, J. Non-Cryst, Solids 356 (2010) 2641–2644.

[33] P.H. Gaskell, M.C. Eckersley, A.C. Barnes, P. Chieux, Nature 350 (1991) 675–677.

[34] M.C. Abramo, C. Caccamo, G. Pizzimenti, Phys. Lett. A 166 (1992) 65–69.

[35] D. Neuville, L. Hennet, Rev. Miner. Geochem 78 (2014) 779–800.

[36] S. Gražulis, D. Chateigner, R.T. Downs, A.F.T. Yokochi, M. Quirós, L. Lutterotti, E. Manakova, J. Butkus, P. Moeck, A. Le Bail, J. Appl. Cryst. 42 (2009) 726–729.